NEURAL REGENERATION RESEARCH
www.nrronline.org

Research Article

Estimation of the density of neural, glial, and endothelial lineage cells in the adult mouse dentate gyrus

https://doi.org/10.4103/1673-5374.327354

Date of submission: January 20, 2021

Date of decision: March 3, 2021

Date of acceptance: April 6, 2021

Date of web publication: November 12, 2021

Joshua D. Rieskamp[1, 2], Patricia Sarchet[2], Bryon M. Smith[2], Elizabeth D. Kirby[2, 3, 4, *]

From the Contents

Graphical Abstract *The cellular composition of the adult mouse dentate gyrus*

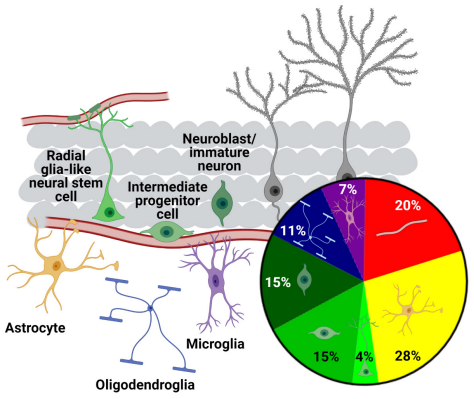

Abstract

The dentate gyrus subregion of the mammalian hippocampus is an adult neural stem cell niche and site of lifelong neurogenesis. Hypotheses regarding the role of adult-born neuron synaptic integration in hippocampal circuit function are framed by robust estimations of adult-born *versus* pre/perinatally-born neuron number. In contrast, the non-neurogenic functions of adult neural stem cells and their immediate progeny, such as secretion of bioactive growth factors and expression of extracellular matrix-modifying proteins, lack similar framing due to few estimates of their number *versus* other prominent secretory cells. Here, we apply immunohistochemical methods to estimate cell density of neural stem/progenitor cells *versus* other major classes of glial and endothelial cell types that are potentially secretory in the dentate gyrus of adult mice. Of the cell types quantified, we found that $GFAP^+SOX2^+$ stellate astrocytes were the most numerous, followed by $CD31^+$ endothelia, $GFAP^-SOX2^+$ intermediate progenitors, $Olig2^+$ oligodendrocytes, $Iba1^+$ microglia, and $GFAP^+SOX2^+$ radial glia-like neural stem cells. We did not observe any significant sex differences in density of any cell population. Notably, neural stem/progenitor cells were present at a similar density as several cell types known to have potent functional roles via their secretome. These findings may be useful for refining hypotheses regarding the contributions of these cell types to regulating hippocampal function and their potential therapeutic uses. All experimental protocols were approved by the Ohio State University Institutional Animal Care and Use Committee (protocol# 2016A00000068) on July 14, 2016.

Key Words: adult neurogenesis; dentate gyrus; endothelia; glia; hippocampus; neural stem cell; secretome; stereology

Chinese Library Classification No. R459.9; R364; Q2

Introduction

The mammalian hippocampus is well studied for its role in episodic memory, spatial navigation, and mood regulation (Strange et al., 2014). Within the hippocampal circuit, the dentate gyrus (DG) subregion mediates crucial computational processes related to memory, such as pattern separation, and affect regulation (Yassa and Stark, 2011; Knierim and Neunuebel, 2016). The DG is unique compared to most adult brain circuits because it hosts a specialized niche where radial glia-like neural stem cells (RGL-NSCs) continuously generate granule neurons throughout life. Adult hippocampal neurogenesis occurs in most mammals, possibly including humans (Gonçalves et al., 2016; Boldrini et al., 2018; Moreno-Jiménez et al., 2019), though recent reports call into question its extent in humans (Sorrells et al., 2018). Rodent studies implicate new granule neurons generated via adult neurogenesis in several key cognitive tasks carried out by the DG (Miller and Sahay, 2019). Furthermore, experimental manipulations that mitigate age-related declines in neurogenesis improve cognitive performance (McAvoy et al., 2016; Berdugo-Vega et al., 2020), raising the possibility that targeting neurogenesis could be therapeutically useful. Therefore, developing a comprehensive picture of the factors that regulate adult hippocampal neurogenesis and how it then contributes to hippocampal function is a topic of intense investigation.

[1]Neuroscience Graduate Program, [2]Department of Psychology, [3]Department of Neuroscience, [4]Chronic Brain Injury Program, The Ohio State University, Columbus, OH, USA

***Correspondence to:** Elizabeth D. Kirby, PhD, kirby.224@osu.edu.
https://orcid.org/0000-0001-9313-3790 (Elizabeth D. Kirby)

Funding: *The study was partially supported by a R00 Pathway to Independence Award from NIH/NINDS (R00NS089938; to EDK).*

How to cite this article: *Rieskamp JD, Sarchet P, Smith BM, Kirby ED (2022) Estimation of the density of neural, glial, and endothelial lineage cells in the adult mouse dentate gyrus. Neural Regen Res 17(6):1286-1292.*

While numerous studies support a functional role of adult-born neurons in the DG, more recently, other functions of RGL-NSCs and their progenitor progeny (neural stem/progenitor cells [NSPCs] all together), beyond generation of new neurons, have emerged. For example, several studies show that adult DG NSPCs have a rich, soluble secretome (Denninger et al., 2020) that can regulate processes such as their own proliferative maintenance (Kirby et al., 2015; Zhou et al., 2018) or neuronal maturation (Tang et al., 2019). Immature neuroblasts have similarly been shown to modulate DG function through a senescent secretome that recruits immune activation (Jin et al., 2021). Adult NSPCs may also modulate the extracellular matrix though cell surface expression of matrix modifying enzymes (Kjell et al., 2020). Cumulatively, these studies reveal unexpected, non-neurogenic functions of NSPCs.

A key step in framing our understanding of the functional relevance of immature neurons has been quantifying their number relative to mature granule neurons (Cameron and McKay, 2001; Jinno and Kosaka, 2010; Jinno, 2011). A similar framing for non-neurogenic functions of NSPCs requires comparison to a broad spectrum of cell types from multiple lineages and is currently lacking. Previous studies quantifying non-neural DG cells mostly report only a select few cell types. As a result, one must combine multiple sources to obtain a comprehensive estimate of DG cell composition. This approach is problematic because cell density estimates vary substantially across studies, even for commonly quantified cell types (Keller et al., 2018), leading to considerably different conclusions depending on which data is used to draw comparisons. In addition, while efforts have been made more recently to generate comprehensive atlases (Erö et al., 2018), these databases currently do not include information about neurogenesis-relevant DG cell types such as NSPCs and vascular endothelial cells.

To create a single assessment of non-neuronal DG cell types in the widely used C57BL/6 mouse model, we use standard immunohistochemical methods in fixed tissue within the same study to estimate the relative densities of radial glial-like NSCs (RGL-NSCs) and their intermediate progenitor cell (IPC) progeny, neuroblasts/immature neurons, oligodendroglial cells, astrocytes, microglia, and vascular endothelial cells in the DG. To our knowledge, this represents the first effort to quantify these cell types from multiple major lineages within a single study and to compare NSPC density to other major classes of secretory cells.

Materials and Methods

Animals

All experimental protocols were performed in accordance with institutional guidelines approved by the Ohio State University Institutional Animal Care and Use Committee (protocol# 2016A00000068, approved on July 14, 2016) and with recommendations of the National Institutes of Health Guide for the Care and Use of Laboratory Animals. C57BL/6 mice (5 males, 4 females) were acquired from Jackson Laboratories at 7 weeks of age and housed in a vivarium at Ohio State University with 24-hour *ad libitum* water and standard mouse chow on a 12-hour light-dark cycle for 1 week. Mice weighed 18–20 g and received one injection of 150 mg/kg bromodeoxyuridine (BrdU; Sigma, St. Louis, MO, USA) dissolved in physiological saline, and 2 hours later were anesthetized with intraperitoneal injections of 87.5 mg/kg ketamine (West-Ward, Eatontown, NJ, USA)/12.5 mg/kg xylazine (Akorn, Lake Forest, IL, USA) and transcardially perfused with 0.1 M phosphate buffered saline (PBS).

Tissue processing and immunohistochemical staining

Brains were fixed for 24 hours in 4% paraformaldehyde in 0.1 M phosphate buffer then equilibrated for at least 2 days in 30% sucrose in 0.1 M PBS, both at 4°C. They were then sliced on a freezing microtome (Leica, Buffalo Grove, IL, USA) in a 1 in 12 series of 40 µm slices. Slices were stored in cryoprotectant at –20°C. Immunohistochemical staining was performed on free-floating sections as previously described (Smith et al., 2018). Briefly, sections were rinsed three times in PBS, incubated in blocking solution (1% normal donkey serum, 0.3% triton-X 100 in PBS) for 30 minutes then incubated in primary antibody (**Table 1**) diluted in blocking buffer overnight at 4°C on rotation. The next day, sections were rinsed and incubated in secondary antibody (**Table 1**) in blocking solution at room temperature for 2 hours, followed by 10 minutes in Hoechst 33342 (Invitrogen, Carlsbad, CA, USA) diluted 1:2000 in PBS. After rinsing, sections were mounted on Superfrost Plus glass slides (Fisher Scientific, Waltham, MA, USA) and cover-slipped with Prolong Gold Anti-fade medium (Invitrogen). After drying, slides were stored in the dark at 4°C until imaging. For BrdU immunohistochemical labeling, the above procedures were followed with the addition of 30-minute incubation in 2 N HCl at 37°C to denature DNA before the blocking step.

Stereological cell counts

Unbiased stereological cell counts were performed in a single series of every 12th slice for each cell phenotype marker. Images of the dorsal DG, anterior-posterior(AP) –1.4 mm to –2.4 mm (Paxinos and Franklin, 2013), were captured using Zeiss AxioImager.M2 microscope and a Zeiss MRc digital camera (Zeiss, Oberkochen, Germany). Cells were counted at 100× (NeuN) or 40× (all other cell types) magnification with oil immersion using the optical fractionator method (StereoInvestigator, MBF Bioscience, Williston, VT, USA). The counting frame had an area of 625 µm^2 (NeuN) or 10,000 µm^2 (all other markers) and a height of 15 µm with 5 µm guard zones. Proliferating cells and oligodendroglial cells were identified using the nuclear markers in **Table 1**. Endothelial cells and microglia were identified by the cytoplasmic markers in **Table 1** surrounding a Hoechst$^+$ nucleus. RGL-NSCs were identified as sex determining region Y-box 2 (SOX2$^+$) nuclei in the subgranular zone (SGZ) surrounded by glial fibrillary acidic protein (GFAP$^+$) cytoplasm with an apical process extending into the granular cell layer. IPCs were identified as SOX2$^+$ nuclei in the SGZ lacking cytoplasmic GFAP. Astrocytes were identified as SOX2$^+$ cells with GFAP$^+$ stellate processes located in any DG subregion.

BrdU colocalization analysis

Colocalization analysis was performed to determine the identity of BrdU-labeled cells. A Zeiss Axio Observer Z.1 with apotome digital imaging system and Axiocam 506 monochrome camera was used to acquire 20 µm z-stack images at 1 µm intervals. BrdU-labeled nuclei in the SGZ were manually analyzed via Zen Blue software (Zeiss) for colocalization with SOX2 and GFAP staining.

Cell density and distribution

Cell density was calculated from total stereological cell count estimate divided by sampled DG tissue volume. Because immunohistochemical processing causes tissue shrinkage, sampled tissue volume was estimated using sampled area adjusted by the proportional change in measured post-processing tissue thickness (i.e. thickness measured in 3 locations per slice using StereoInvestigator *versus* the sliced thickness of 40 µm).

Incomplete antibody penetration can interfere with obtaining accurate stereological estimates. We verified complete antibody penetration by comparing the number of cells for each maker counted in five consecutive 1 µm z-sections in the middle of the tissue compared to the 5 consecutive 1 µm z-sections immediately below the guard zone (top). We observed similar counts obtained from the middle z-sections compared to the top, suggesting uniform antibody penetration.

Table 1 | **Antibodies used for immunohistochemical identification of cell phenotype**

Antibody	Host species	Cell type	Antigen retrieval	Vendor/Product#	RRID	Dilution	Reference/Control
Primary antibodies							
Anti-SOX2	Rat	RGL, IPC, astrocyte	None	eBioscience 14-9811	AB_2865465	1:1000	Andersson-Rolf et al., 2017
Anti-GFAP	Rabbit	RGL, astrocyte	None	Dako Z-0334	AB_10013382	1:1000	Michalovicz et al., 2019
Anti-MCM2	Rabbit	Proliferating cells	None	Cell Signaling 4007	AB_2142134	1:500	Wang et al., 2017
Anti-BrdU	Mouse	Proliferating cells	2 N HCl, 37°C	BD Biosciences BDB 347580	AB_10015219	1:500	No BrdU injection
Anti-DCX	Rabbit	Neuroblast/ immature neuron	None	Cell Signaling 4604	AB_561007	1:500	Tang et al., 2019
Anti-NeuN	Mouse	Mature Neuron	None	EMD Milipore MAB377	AB_2298772	1:500	Buscemi et al., 2019
Anti-Iba1	Goat	Microglia	None	Abcam Ab5076	AB_2224402	1:2000	Smith et al., 2018
Anti-CD31	Rat	Endothelia	None	BD Pharmingen 550274	AB_393571	1:100	Buscemi et al., 2019
Anti-Olig2	Mouse	Oligodendroglia lineage	None	EMD Millipore MABN50	AB_10807410	1:1000	Valério-Gomes et al., 2018
Secondary antibodies							
647 anti-rabbit	Donkey	GFAP, MCM2	N/A	Invitrogen A31573	AB_2536183	1:500	No primary
594 anti-rat	Donkey	SOX2, CD31	N/A	Invitrogen A21209	AB_2535795	1:500	No primary
488 anti-mouse	Donkey	BrdU, NeuN	N/A	Invitrogen A21202	AB_141607	1:500	No primary
488 anti-goat	Donkey	Iba1	N/A	Invitrogen A11055	AB_2534102	1:500	No primary
555 anti-mouse	Donkey	Olig2	N/A	Invitrogen A31570	AB_2536180	1:500	No primary

All antibodies were validated in previous work or compared to an appropriate control to ensure specificity of immunolabeling. BrdU: Bromodeoxyuridine; CD31: cluster of differentiation 31; DCX: doublecortin; GFAP: glial fibrillary acidic protein; Iba1: ionized calcium-binding adapter molecule 1; IPC: intermediate progenitor cell; MCM2: minichromosome maintenance 2; NeuN: neuronal nuclear protein; Olig2: oligodendrocyte transcription factor 2; RGL: radial glia-like; SOX2: (sex determining region Y)-box 2.

Error estimates

As previous work suggests that the Gundersen-Jensen coefficient of error (CE) estimator (Gundersen et al., 1999) is useful for evaluating the precision of stereological estimates in the hippocampal structure (Slomianka and West, 2005), we calculated the mean Gundersen-Jensen CE for each cell type using Stereoinvestigator.

Statistics

For each cell type, cell densities in males and females were compared using an unpaired, two-tailed *t*-test. As no significant sex differences were detected, cell densities were combined across males and females and compared using one-way analysis of variance (ANOVA) followed by Tukey's *post hoc* analysis to test for significant differences in cell density between cell types. Because NeuN cell density was at least 10-fold greater than any other cell marker, we excluded it from the ANOVA as it would potentially obscure differences between other cell types. Statistical analyses were performed in Prism version 8 (Graphpad Software, San Diego, CA, USA), except for power analysis which was performed using G*power version 3.1 (Faul et al., 2007).

Results

We used immunohistochemistry to identify cells across all layers of the DG expressing phenotypic markers of major DG lineages: neural, astroglial, oligodendroglial, microglial, and vascular endothelial (**Figure 1**). The mean number of cells counted, measured tissue thickness, distribution of cells throughout the tissue thickness, and Gundersen-Jensen error estimates are reported in **Table 2**.

NSPCs and astroglia

Because many of the protein markers expressed by adult neural precursors are also present in mature astrocytes (Semerci and Maletic-Savatic, 2016), we distinguished these cell populations based on a combination of SOX2 and GFAP immunolabeling along with cell morphology (Suh et al., 2007; **Figure 2Ai–iv**). As expected, RGL-NSC cell bodies were solely located in the subgranular zone (SGZ) with a radial/apical process extending into the granule cell layer (**Figure 2Aiii**). The IPC progeny of RGL-NSCs were also located in the SGZ (**Figure 2Aiii**). Mature protoplasmic astrocytes with $SOX2^+$ nuclei were located in all regions of the DG (**Figure 2Aiv**). We found that mature astrocytes were the most abundant of these three populations (8274.7 ± 1109.7, 9232.4 ± 1095.1 cells/mm^3, females and males, respectively) followed by IPCs (4532.2 ± 469.7, 5220.1 ± 820.2 cells/mm^3), then RGL-NSCs (1364.9 ± 132.0, 1228.6 ± 59.5 cells/mm^3, **Figure 3A**). Males and females did not significantly differ in number of astrocytes (t = 0.61, P > 0.05), RGLs (t = 1.02, P > 0.05), or IPCs (t = 0.68, P > 0.05).

Mitotically active cells

To expand the quantification of progenitor cells, we used two markers of cellular mitosis. The adult DG contains various populations of mitotically active cells, which can be identified using endogenous cell cycle markers such as minichromosome maintenance 2 (MCM2) or the exogenous S phase marker bromodeoxyuridine (BrdU) (von Bohlen und Halbach, 2011; Kuhn et al., 2016). Previous studies have shown that the majority of $MCM2^+$ or acutely BrdU-labeled cells in the DG are IPCs located within the SGZ, with a sparser number of proliferative glial cells located outside the SGZ (Mandyam et al., 2007; Bonaguidi et al., 2011). Consistent with these previous findings, we found $MCM2^+$ cells throughout the entire DG, but the greatest density was found within the SGZ (**Figure 2Bi–iii**). To obtain counts most directly related to IPC number, only $MCM2^+$ cells in the SGZ were quantified. The density of $MCM2^+$ cells in the SGZ did not significantly differ between females and males (4324.1 ± 1106.9 *vs.* 3740.7 ± 356.8 cells/mm^3; t = 0.55, P > 0.05) (**Figure 3A**). We obtained similar results quantifying $BrdU^+$ cells after a single BrdU injection 2 hours before perfusion. BrdU labeled cells were found throughout the entire extent of the DG, but most commonly within the SGZ (**Figure 2Ci–iii**). The density of BrdU-labeled cells in the SGZ was not different between females and males (658.4 ± 61.9 *vs.* 597.3 ± 162.1 cells/mm^3; t = 0.32, P > 0.05) and represented a smaller subset of cells than all cycling (i.e. $MCM2^+$) cells, as expected (**Figure 3A**). Colocalization analysis revealed that ~88% of BrdU-labeled cells in the SGZ were $SOX2^+GFAP^-$ putative IPCs (87.9 ± 1.2% females, 88.7 ± 1.3% males, **Figure 3F**), consistent with previous studies (Encinas et al., 2011), which suggests that counts of $BrdU^+$ cells in the SGZ are most directly related to

Table 2 | **Total counts, distribution, error estimators, measured tissue thickness, and number of sections sampled for all cell types**

Cell type marker	Total cells counted	Distribution (% of all counted cells)		Gundersen-Jensen CE (m = 0)	Gundersen-Jensen CE (m = 1)
		Top 5 µm	Middle 5 µm		
$GFAP^+SOX2^+$ stellate	308.1±7.5	32.32±0.95	37.55±0.73	0.144	0.064
$GFAP^+SOX2^+$ radial	46.4±4.1	34.44±1.75	33.48±2.37	0.203	0.154
$GFAP^-SOX2^+$	148.3±8.2	30.07±2.17	36.06±1.83	0.164	0.088
MCM2	140.1±10.5	38.47±3.69	33.63±2.52	0.188	0.094
BrdU	22.7±2.7	37.25±5.32	20.58±5.46	0.287	0.243
DCX	217.6±14.7	33.27±2.67	34.94±1.88	0.161	0.078
NeuN	325.8±21.6	36.60±1.15	37.80±0.88	0.183	0.068
Iba1	74.3±6.6	35.49±0.76	34.75±1.76	0.164	0.12
CD31	175.1±7.7	30.21±1.15	39.07±1.97	0.161	0.083
Olig2	111.6±10.6	35.99 ± 4.06	33.05±3.02	0.169	0.101

Immunostaining round	Measured tissue thickness		Sections surveyed	Sites surveyed
	Males	Females		
GFAP, SOX2, BrdU	25.3±0.09	26.6±1.33	3	56.8±1.3
DCX, NeuN, CD31	25.9±0.80	24.8±0.75	3	60.6±1.3
MCM2, Olig2, Iba1	26.3±0.69	25.5±0.86	3	59.7±1.5

For each cell type, the total cells counted and percentage of cells counted in the middle 5 consecutive 1 µm z-sections and top 5 consecutive 1 µm z-sections immediately below the guard zone are listed (mean ± SEM). Error estimators are listed as Gundersen-Jensen coefficients (CE) (with smoothness m = 0 or m = 1). For each round of immunostaining, the measured thickness (mean ± SEM) and number of sections sampled is provided. Thickness was manually measured in 3 locations per slice to adjust for shrinkage relative to the 40 µm starting thickness. BrdU: Bromodeoxyuridine; CD31: cluster of differentiation 31; DCX: doublecortin; GFAP: glial fibrillary acidic protein; Iba1: ionized calcium-binding adapter molecule 1; MCM2: minichromosome maintenance 2; NeuN: neuronal nuclear protein; Olig2: oligodendrocyte transcription factor 2; SOX2: (sex determining region Y)-box 2.

numbers of IPCs in S phase. BrdU-labeled cells outside of the SGZ could represent glial progenitor cells in S phase but were too sparse for reliable quantification.

Neuroblasts/immature neurons and mature neurons

In the DG, doublecortin (DCX) marks neuroblasts (NBs) and recently born, immature granule neurons (INs), while NeuN marks the nuclei of various mature neuronal subtypes, the most abundant of which is mature granule neurons (Kuhn et al., 2016). As expected, DCX^+ cells were located within the SGZ and inner third of the granular cell layer (**Figure 2Di–iii**). The density of DCX^+ cells was similar in scale to $MCM2^+$ and $SOX2^+$ IPCs and did not significantly differ between females and males (4820.5 ± 656.4 *vs*. 4924.7 ± 376.0 cells/mm^3, t = 0.15, P > 0.05; **Figure 3A**). Mature $NeuN^+$ neurons were located mostly within the GCL, likely representing granule neurons, with sparse cells in the hilus and molecular layer, likely representing hilar mossy neurons and various subclasses of interneuron (**Figure 2Ei–iii**). The density of NeuN+ cells was at least 10-fold greater than that of all other cell types quantified here and did not significantly differ by sex (100,564.5 ± 21,696.6 *vs*. 115,109.3 ± 29,242.0, females *vs*. males, t = 0.24, P > 0.05; **Figure 3C**).

Oligodendroglial cells

We identified cells of the oligodendroglia lineage including oligodendrocyte progenitor cells, newly formed oligodendrocytes, and mature myelinating oligodendrocytes based on Olig2 immunolabeling (Valério-Gomes et al., 2018). $Olig2^+$ cells were mainly distributed throughout the molecular layer and hilus of the DG (**Figure 2Fi–iii**). The density of oligodendroglia lineage cells was most similar to that of $MCM2^+$ and $SOX2^+$ IPCs as well as DCX^+ NB/INs and not different between females and males (4125.9 ± 1213.0 *vs*. 2610.7 ± 333.1 cells/mm^3, t = 1.34, P > 0.05; **Figure 3A**).

Microglia

To quantify microglia, we used Iba1 immunolabeling, which can also detect resident perivascular or infiltrating macrophages. However, in the DG of healthy, young mice, Iba1 labeling is most directly linked to microglia number as infiltrating macrophages are rare and perivascular macrophages occupy a specific spatial compartment around blood vessels distinct from parenchyma-residing microglia (Galea et al., 2005). $Iba1^+$ cells were distributed throughout every region of the DG (**Figure 2Gi–iii**) and were intermediate in density between oligodendroglial lineage cells and IPCs and RGLs. No sex difference was found in $Iba1^+$ cell density (2677.1 ± 892.1 *vs*. 1816.8 ± 210.2 cells/mm^3, females *vs*. males, t = 1.05, P > 0.05; **Figure 3A**).

Vascular endothelial cells

Vascular endothelial cells within the DG were identified by CD31 immunolabeling and formed vascular networks throughout all regions of the DG (**Figure 2Hi–iii**). The density of $CD31^+$ cells was most similar to $SOX2^+$ IPCs and DCX^+ NB/INs, with no sex difference (6768.7 ± 1067.3 *vs*. 5849.0 ± 639.4 cells/mm^3, females *vs.* males, t = 0.78, P > 0.05; **Figure 3A**).

Cellular composition of the DG

Cell density estimates for each cell marker quantified in the current study are depicted in **Figure 3A** and **C**. The results of statistical analysis for differences in cell density between cell types are depicted in **Figure 3E**. To facilitate comparisons with counts performed in sections cut to a commonly used thickness for free-floating immunohistochemistry, data is also presented as estimates of cell number in a 40 µm slice (**Figure 3B** and **D**). We also determined the relative cell densities across the anterior-posterior extent of the dorsal DG (**Figure 3G**). $GFAP^+SOX2^+$ stellate astrocytes and $CD31^+$ endothelia were the only cell types to show variance by anatomical position, both decreasing in density at the posterior pole of the dorsal DG. We did not detect significant sex differences for any of the cell types quantified. To understand the robustness of this finding, we used our data to inform power analyses to estimate sample size required to detect sex differences in each cell type density. Using our data to estimate means and pooled variance, we found that the sample sizes required to detect sex differences with 80% power and alpha of 0.05 were substantially larger than those used in the present study (**Table 3**). Our sample size would need to increase by 4 to > 300 fold to be powered for detection of sex differences using the current methodology.

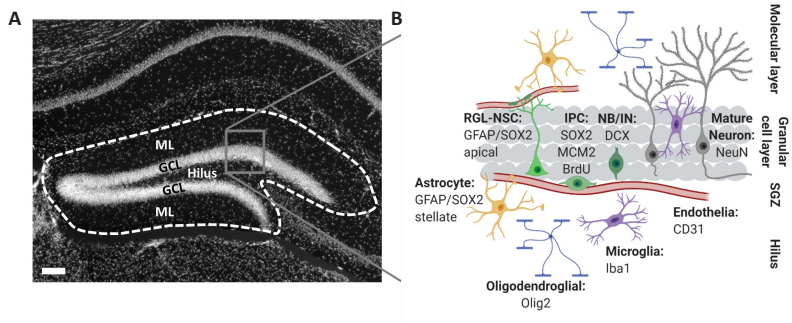

Figure 1 | Cell locations and phenotypes sampled.
(A) The region of interest used (dashed outline) for cell counts encompassed all layers of the dorsal DG, including the supra and infrapyramidal molecular layer (ML), granular cell layer (GCL) and subgranular zone (SGZ), as well as the hilus. Hoechst labels cell nuclei. Scale bar: 100 µm. (B) Schematic of the cell types quantified in this study and their relative locations within the DG. Vascular endothelial cells (red), astrocytes (yellow), radial glia-like neural stem cells (RGL-NSCs, green with single process), intermediate progenitor cells (IPCs, green, bipolar horizontal), neuroblasts/immature neurons (NB/INs, green, bipolar vertical), mature neurons (gray), oligodendroglial cells (blue), and microglia (purple). Created using BioRender.com. BrdU: Bromodeoxyuridine; CD31: cluster of differentiation 31; DCX: doublecortin; GFAP: glial fibrillary acidic protein; Iba1: ionized calcium-binding adapter molecule 1; MCM 2: minichromosome maintenance 2; NeuN: neuronal nuclear protein; Olig2: oligodendrocyte transcription factor 2; SOX2: (sex determining region Y)-box 2.

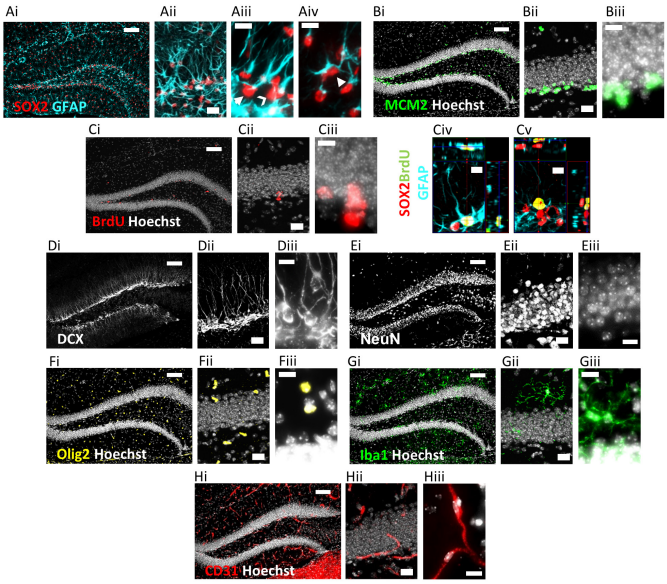

Figure 2 | Representative images of immunolabeling for all cell types surveyed.
(Ai–iv) Representative SOX2 and GFAP immunolabeling. Radial glia-like neural stem cells (RGL-NSCs) had SOX2$^+$ nuclei in the subgranular zone (SGZ), GFAP$^+$ cytoplasm, and a radial/apical process spanning the granular cell layer (Aiii, arrow). Intermediate progenitor cells (IPCs) had SOX2$^+$ nuclei in the SGZ lacking GFAP$^+$ cytoplasm (Aiii, chevrons). Mature astrocytes had SOX2$^+$ nuclei, GFAP$^+$ cytoplasm, and stellate morphology (Aiv, arrow). (Bi–iii) Minichromosome maintenance 2 (MCM2) immunolabeling and (Ci–iii) BrdU immunolabeling 2 hours post injection to reveal actively cycling cells. Orthogonal projections showing a putative RGL with colocalized BrdU$^+$SOX2$^+$ nucleus and GFAP$^+$ radial process (Civ) and a putative IPC with colocalized BrdU$^+$SOX2$^+$ nucleus lacking GFAP (Cv). (Di–iii) Representative immunolabeling of DCX$^+$ neuroblasts/immature neurons. (Ei–iii) NeuN immunolabeling to detect mature neurons (Fi–iii) Olig2 immunolabeling to detect oligodendroglial lineage cells. (Gi–iii) Representative Iba1 immunolabeling for microglia. (Hi–iii) CD31 immunolabeling to detect vascular endothelial cells. Scale bars represent 100 µm (i panels), 20 µm (ii panels), or 10 µm (iii–v panels). BrdU: Bromodeoxyuridine; GFAP: glial fibrillary acidic protein; SOX2: (sex determining region Y)-box 2.

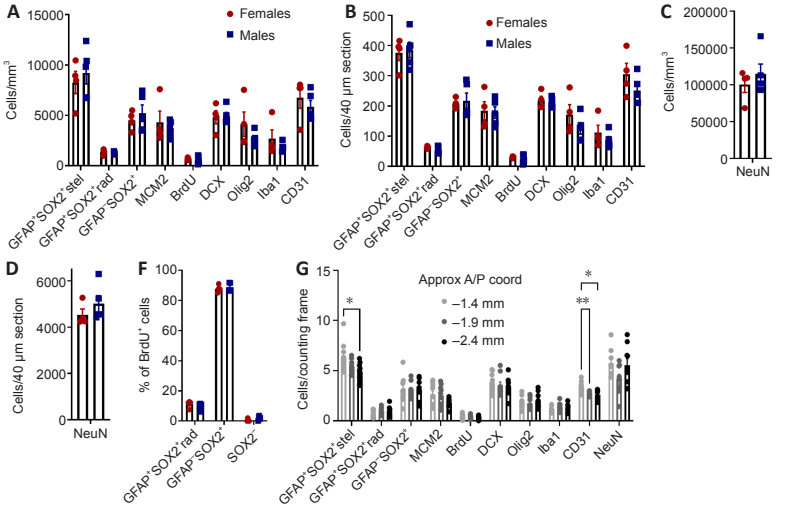

E

	Astro	RGL	IPC	MCM2	BrdU	DCX	Olig2	Iba1	CD31
Astro		****	****	****	****	****	****	****	**
RGL	****		****	**	ns	****	ns	ns	****
IPC	****	****		ns	****	ns	ns	**	ns
MCM2	****	**	ns		***	ns	ns	ns	*
BrdU	****	ns	****	***		****	**	ns	****
DCX	****	****	ns	ns	****		ns	**	ns
Olig2	****	ns	ns	ns	**	ns		ns	**
Iba1	****	ns	**	ns	ns	**	ns		****
CD31	**	****	ns	*	****	ns	**	****	

Figure 3 | Quantification of astroglial, neural stem and progenitor cell, neuroblast/immature and mature neuronal, oligodendroglial, microglial, and endothelial cell density in the dentate gyrus.
Quantification is represented as cell density (A, C) and number of cells in a 40 µm coronal slice (B, D). Data are mean ± SEM from male (n = 5) and female (n = 4) adult mice. No significant sex difference for any cell type was detected via unpaired, two-tailed t-test ($P > 0.05$). (E) Matrix table showing results of one-way analysis of variance (ANOVA) with Tukey's *post hoc* comparisons between cell type densities, combined across males and females, *$P < 0.05$, **$P < 0.01$, ***$P < 0.001$, ****$P < 0.0001$. (F) Identity of BrdU-labeled cells within the SGZ is shown as % of all BrdU-labeled cells colocalizing with the given markers. (G) Number of cells per counting frame across the anterior-posterior (A-P) extent of the dorsal dentate gyrus, divided into 3 bins by A-P coordinate, analyzed by two-way repeated measures ANOVA with Tukey's *post hoc* comparisons, *$P < 0.05$,**$P < 0.01$. Astro: Astrocyte; BrdU: bromodeoxyuridine; CD31: cluster of differentiation 31; DCX: doublecortin; GFAP: glial fibrillary acidic protein; Iba1: ionized calcium-binding adapter molecule 1; IPC: intermediate progenitor cell; MCM 2: minichromosome maintenance 2; NeuN: neuronal nuclear protein; ns: not significant; Olig2: oligodendrocyte transcription factor 2; rad: radial; RGL: radial glia-like; SOX2: (sex determining region Y)-box 2; stel: stellate.

Table 3 | **Power analysis to detect sex differences**

Cell type	Pooled SD	Calculated *n* for 80% power, alpha 0.05
$GFAP^+SOX2^+$ stellate	2353.11	95
$GFAP^+SOX2^+$ radial	199.98	34
$GFAP^-SOX2^+$	1516.59	77
MCM2	1569.81	114
BrdU	285.80	344
DCX	1068.90	1652
Olig2	1684.96	20
Iba1	1220.89	32
CD31	1441.90	39

For each cell type, the sample size required to detect significant differences between males and females based on obtained counts and variance was calculated for 80% power with alpha = 0.05. BrdU: Bromodeoxyuridine; CD31: cluster of differentiation 31; DCX: doublecortin; GFAP: glial fibrillary acidic protein; Iba1: ionized calcium-binding adapter molecule 1; MCM2: minichromosome maintenance 2; Olig2: oligodendrocyte transcription factor 2; SOX2: (sex determining region Y)-box 2.

Discussion

Adult hippocampal neurogenesis in rodents occurs within the DG, a niche comprised of multiple cell types including neural, glial, and endothelial cells. Previous work characterizing the relative cell population sizes of the neurogenic lineage has focused on the number of newborn neurons relative to mature granule neurons (Cameron and McKay, 2001; Jinno and Kosaka, 2010; Jinno, 2011). For example, in the ongoing debate about existence and relevance of adult hippocampal neurogenesis in humans, the relative numbers of adult-generated neurons versus developmentally generated neurons is an issue of intense focus (Spalding et al., 2013). Previous estimates suggest that adult born, immature neurons represent less than 10% of total DG excitatory neurons (Cameron and McKay, 2001; Spalding et al., 2013), and this number is sufficient to modulate DG circuit activity (Miller and Sahay, 2019). This focus on neuronal progeny derives from the assumption that the function of NSPCs relies solely on the electrophysiological activity of newly born neurons. However, emerging evidence supports multiple non-neurogenic functions of endogenous NSPCs such as via secretion of soluble growth factors (Bacigaluppi et al., 2020) and cell-surface enzymes (Kjell et al., 2020). There is also growing evidence that stem cell transplants in the adult brain may achieve therapeutic effect via their secretome (Willis et al., 2020). Here, we sought to quantify several non-neuronal cell types of the adult DG to generate a useful resource for researchers to reference as new functional roles of NSPCs are identified that require their comparison to various other cell types.

While previous studies have estimated population size for each of the DG cell types studied here individually, comparison of our data with previous work is complicated by the variability in population estimates across studies (Keller et al., 2018). For example, estimates of astrocyte density in the DG range from 19,900 cells/mm^3 (Ogata and Kosaka, 2002) to 55,700 cells/mm^3 (Long et al., 1998). Despite these studies both using unbiased stereology, variability could arise for biological (different cohorts of mice), methodological (different markers and anatomical boundaries), and computational (different extrapolation from sampled counts to total population density estimates) reasons. Even small differences in sampling parameters and adjustments for tissue shrinkage become amplified when calculating estimates of total population size and tissue volume (Keller et al., 2018). How the data derived from differing methods can be adjusted for comparison is not immediately clear. This variability combined with the tendency of most studies to examine a select few cell types complicates attempts to compare cell population sizes across studies.

To circumvent these issues, we sought to use consistent methodology to obtain estimates for a comprehensive set of DG cell types. All data in this study were generated using tissue from a single cohort of male and female mice of the C57BL/6 strain, one of the most commonly used rodent species in biosciences research (Bryant, 2011). Therefore, the main advantage of this dataset is the validity of internal comparisons between various cell types in a common research model species. For example, when drawing comparisons based on data reported in separate studies, the microglia to astrocyte ratio could range from approximately 1:1 (Long et al., 1998; Ogata and Kosaka, 2002) to 1:6 (Mouton et al., 2002; Wirenfeldt et al., 2003). In comparison, using our estimates, we report a microglia to astrocyte ratio of roughly 1:4, similar to the approximately 1:3 ratio reported by others when both cell types were quantified within the same study (Long et al., 1998; Mouton et al., 2002). This test case highlights the utility of counts obtained within a single study for making accurate comparisons of relative population sizes.

When comparing NSPCs to several major classes of secretory cells, we found that NSPCs exist in similar abundance as other major cell types that are well-known to regulate the function of the DG via their secretome. We found that $GFAP^+SOX2^+$ stellate astrocytes were the largest cell population of those included in our study, followed closely by vascular endothelial cells. IPCs and neuroblasts/immature neurons were the next most abundant, being present at about half the density of astrocytes. Oligodendroglial cells and microglia were present at a quarter to a third the density of astrocytes. RGL-NSCs were the least abundant cell population, being ~85% less abundant than astrocytes. However, NSPCs together (RGL-NSCs and IPCs) represented a cell population ~30% less abundant than astrocytes and over 250% more abundant than microglia.

There are many factors that can modulate the functional impact of a cell population's secretome, including: number of cells in that population, number of cells in other, nearby secretory populations, quantity of proteins secreted per cell, quantity of the same proteins secreted by other cells, and the relative solubility/bioavailability of individual secreted proteins. This study addresses the first two factors—providing relative densities of major cell types in the DG which may influence their environment through their secretome. Specifically for NSPCs, our data show that within the adult DG, NSPC total density is similar in scale to other cell populations believed to be important secretome contributors. Future work is needed, however, to expand on this data and more directly quantify the contribution of NSPCs to the DG secretome and its functional significance relative to other secretory cell types.

Important limitations to this dataset should be noted. First, while the present study includes data from males and females using sample sizes typical of stereology studies (Mouton et al., 2002; Jinno, 2011), power analysis reveals that this sample size is not large enough to power detection of any potential sex differences in our measures at standard levels of power (80%) and alpha (0.05). In fact, our data suggests that reliably detecting sex differences in the density of cell types surveyed here within the DG requires samples of between 20 (Olig2) and 1652 (DCX) mice. Second, counts were performed in the dorsal DG with no separate delineation of the layers (i.e. molecular, granular, hilar). Future studies could more finely resolve the relative contribution of cell types within more stringently defined microenvironments. For example, when considering cell populations that contribute soluble proteins with short diffusion distances or matrix modifying enzymes, the relative cellular densities might only be meaningful within a small microenvironment, not across the entire DG. Additionally, similar comprehensive analysis of cell types in other adult neural stem cell niches such as the subventricular zone and hypothalamus could elucidate region-specific

cellular composition. This could be a useful starting point for studying changes in neurogenic niche cellular composition with normal aging, disease, or injury. Third, other cell types and subtypes not quantified in our data could be added to create a more complete characterization of all cell types in the adult DG, such as mature inhibitory and excitatory neurons, subdivisions of oligodendrocyte lineage stages (precursor, immature, pre-myelinating, mature), other immune-lineage cells (macrophages, T cells), and other perivascular cells (e.g. pericytes).

In summary, we have provided density estimates for the major cell types of the DG. Our data facilitate direct comparisons of multiple cell types and suggest that NSPCs are present in sufficient abundance to contribute to the DG secretome in biologically meaningful ways. We expect these findings will be useful for refining hypotheses about the relative contributions of these cell types to regulating hippocampal function and their potential therapeutic uses.

Acknowledgments: *The authors would like to thank Dr. Kathryn Lenz for use of equipment.*
Author contributions: *Definition of intellectual content, literature search, data analysis, statistical analysis, manuscript preparation, manuscript editing & manuscript review: JDR. Data acquisition and manuscript review: PS and BMS. Definition of intellectual content, data acquisition, data analysis, statistical analysis, manuscript editing & manuscript review: EDK. All authors approved the final version of the manuscript.*
Conflicts of interest: *The authors declare no conflicts of interest.*
Financial support: *The study was partially supported by a R00 Pathway to Independence Award from NIH/NINDS (R00NS089938; to EDK).*
Institutional review board statement: *All experimental protocols were approved by the Ohio State University Institutional Animal Care and Use Committee (protocol# 2016A00000068) on July 14, 2016.*
Author statement: *This paper has been posted as a preprint on bioRxiv with doi: https://doi.org/10.1101/847350, which is available from: https://www.biorxiv.org/content/10.1101/847350v2.full.*
Copyright license agreement: *The Copyright License Agreement has been signed by all authors before publication.*
Data sharing statement: *Datasets analyzed during the current study are available from the corresponding author on reasonable request.*
Plagiarism check: *Checked twice by iThenticate.*
Peer review: *Externally peer reviewed.*

References

Andersson-Rolf A, Mustata RC, Merenda A, Kim J, Perera S, Grego T, Andrews K, Tremble K, Silva JCR, Fink J, Skarnes WC, Koo BK (2017) One-step generation of conditional and reversible gene knockouts. Nat Methods 14:287-289.
Bacigaluppi M, Sferruzza G, Butti E, Ottoboni L, Martino G (2020) Endogenous neural precursor cells in health and disease. Brain Res 1730:146619.
Berdugo-Vega G, Arias-Gil G, López-Fernández A, Artegiani B, Wasielewska JM, Lee C-C, Lippert MT, Kempermann G, Takagaki K, Calegari F (2020) Increasing neurogenesis refines hippocampal activity rejuvenating navigational learning strategies and contextual memory throughout life. Nat Commun 11:135.
Boldrini M, Fulmore CA, Tartt AN, Simeon LR, Pavlova I, Poposka V, Rosoklija GB, Stankov A, Arango V, Dwork AJ, Hen R, Mann JJ (2018) Human hippocampal neurogenesis persists throughout aging. Cell Stem Cell 22:589-599.e5.
Bonaguidi MA, Wheeler MA, Shapiro JS, Stadel RP, Sun GJ, Ming G, Song H (2011) In vivo clonal analysis reveals self-renewing and multipotent adult neural stem cell characteristics. Cell 145:1142-1155.
Bryant CD (2011) The blessings and curses of C57BL/6 substrains in mouse genetic studies. Ann N Y Acad Sci 1245:31-33.
Buscemi L, Price M, Bezzi P, Hirt L (2019) Spatio-temporal overview of neuroinflammation in an experimental mouse stroke model. Sci Rep 9:507.
Cameron HA, Mckay RDG (2001) Adult neurogenesis produces a large pool of new granule cells in the dentate gyrus. J Comp Neurol 435:406-417.
Denninger JK, Chen X, Turkoglu AM, Sarchet P, Volk AR, Rieskamp JD, Yan P, Kirby ED (2020) Defining the adult hippocampal neural stem cell secretome: In vivo versus in vitro transcriptomic differences and their correlation to secreted protein levels. Brain Res 1735:146717.
Encinas JM, Michurina TV, Peunova N, Park JH, Tordo J, Peterson DA, Fishell G, Koulakov A, Enikolopov G (2011) Division-coupled astrocytic differentiation and age-related depletion of neural stem cells in the adult hippocampus. Cell Stem Cell 8:566-579.
Erö C, Gewaltig MO, Keller D, Markram H (2018) A cell atlas for the mouse brain. Front Neuroinform 12:84.
Faul F, Erdfelder E, Lang AG, Buchner A (2007) G*Power 3: A flexible statistical power analysis program for the social, behavioral, and biomedical sciences. Behav Res Methods 39:175-191.
Paxinos G, Franklin KBJ (2013) Paxinos and Franklin's the mouse brain in stereotaxic coordinates, 4th ed. Boston: Elsevier/Academic Press.
Galea I, Palin K, Newman TA, Van Rooijen N, Perry VH, Boche D (2005) Mannose receptor expression specifically reveals perivascular macrophages in normal, injured, and diseased mouse brain. Glia 49:375-384.
Gonçalves JT, Schafer ST, Gage FH (2016) Adult neurogenesis in the hippocampus: from stem cells to behavior. Cell 167:897-914.
Gundersen HJ, Jensen EB, Kiêu K, Nielsen J (1999) The efficiency of systematic sampling in stereology--reconsidered. J Microsc 193(Pt 3):199-211.
Jin WN, Shi K, He W, Sun JH, Van Kaer L, Shi FD, Liu Q (2021) Neuroblast senescence in the aged brain augments natural killer cell cytotoxicity leading to impaired neurogenesis and cognition. Nat Neurosci 24:61-73.
Jinno S (2011) Topographic differences in adult neurogenesis in the mouse hippocampus: A stereology-based study using endogenous markers. Hippocampus 21:467-480.
Jinno S, Kosaka T (2010) Stereological estimation of numerical densities of glutamatergic principal neurons in the mouse hippocampus. Hippocampus 20:829-840.
Keller D, Erö C, Markram H (2018) Cell densities in the mouse brain: a systematic review. Front Neuroanat 12:83.
Kirby ED, Kuwahara AA, Messer RL, Wyss-Coray T (2015) Adult hippocampal neural stem and progenitor cells regulate the neurogenic niche by secreting VEGF. Proc Natl Acad Sci U S A 112:4128-4133.
Kjell J, Fischer-Sternjak J, Thompson AJ, Friess C, Sticco MJ, Salinas F, Cox J, Martinelli DC, Ninkovic J, Franze K, Schiller HB, Götz M (2020) Defining the adult neural stem cell niche proteome identifies key regulators of adult neurogenesis. Cell Stem Cell 26:277-293.e8.
Knierim JJ, Neunuebel JP (2016) Tracking the flow of hippocampal computation: Pattern separation, pattern completion, and attractor dynamics. Neurobiol Learn Mem 129:38-49.
Kuhn HG, Eisch AJ, Spalding K, Peterson DA (2016) Detection and phenotypic characterization of adult neurogenesis. Cold Spring Harb Perspect Biol 8:a025981.
Long JM, Kalehua AN, Muth NJ, Calhoun ME, Jucker M, Hengemihle JM, Ingram DK, Mouton PR (1998) Stereological analysis of astrocyte and microglia in aging mouse hippocampus. Neurobiol Aging 19:497-503.
Mandyam CD, Harburg GC, Eisch AJ (2007) Determination of key aspects of precursor cell proliferation, cell cycle length and kinetics in the adult mouse subgranular zone. Neuroscience 146:108-122.
McAvoy KM, Scobie KN, Berger S, Russo C, Guo N, Decharatanachart P, Vega-Ramirez H, Miake-Lye S, Whalen M, Nelson M, Bergami M, Bartsch D, Hen R, Berninger B, Sahay A (2016) Modulating neuronal competition dynamics in the dentate gyrus to rejuvenate aging memory circuits. Neuron 91:1356-1373.
Michalovicz LT, Kelly KA, Vashishtha S, Ben-Hamo R, Efroni S, Miller JV, Locker AR, Sullivan K, Broderick G, Miller DB, O'Callaghan JP (2019) Astrocyte-specific transcriptome analysis using the ALDH1L1 bacTRAP mouse reveals novel biomarkers of astrogliosis in response to neurotoxicity. J Neurochem 150:420-440.
Miller SM, Sahay A (2019) Functions of adult-born neurons in hippocampal memory interference and indexing. Nat Neurosci 22:1565-1575.
Moreno-Jiménez EP, Flor-García M, Terreros-Roncal J, Rábano A, Cafini F, Pallas-Bazarra N, Ávila J, Llorens-Martín M (2019) Adult hippocampal neurogenesis is abundant in neurologically healthy subjects and drops sharply in patients with Alzheimer's disease. Nat Med 25:554-560.
Mouton PR, Long JM, Lei DL, Howard V, Jucker M, Calhoun ME, Ingram DK (2002) Age and gender effects on microglia and astrocyte numbers in brains of mice. Brain Res 956:30-35.
Ogata K, Kosaka T (2002) Structural and quantitative analysis of astrocytes in the mouse hippocampus. Neuroscience 113:221-233.
Semerci F, Maletic-Savatic M (2016) Transgenic mouse models for studying adult neurogenesis. Front Biol 11:151-167.
Slomianka L, West MJ (2005) Estimators of the precision of stereological estimates: An example based on the CA1 pyramidal cell layer of rats. Neuroscience 136:757-767.
Smith BM, Yao X, Chen KS, Kirby ED (2018) A larger social network enhances novel object location memory and reduces hippocampal microgliosis in aged mice. Front Aging Neurosci 10:142.
Sorrells SF, Paredes MF, Cebrian-Silla A, Sandoval K, Qi D, Kelley KW, James D, Mayer S, Chang J, Auguste KI, Chang EF, Gutierrez AJ, Kriegstein AR, Mathern GW, Oldham MC, Huang EJ, Garcia-Verdugo JM, Yang Z, Alvarez-Buylla A (2018) Human hippocampal neurogenesis drops sharply in children to undetectable levels in adults. Nature 555:377-381.
Spalding KL, Bergmann O, Alkass K, Bernard S, Salehpour M, Huttner HB, Boström E, Westerlund I, Vial C, Buchholz BA, Possnert G, Mash DC, Druid H, Frisén J (2013) Dynamics of hippocampal neurogenesis in adult humans. Cell 153:1219-1227.
Strange BA, Witter MP, Lein ES, Moser EI (2014) Functional organization of the hippocampal longitudinal axis. Nat Rev Neurosci 15:655-669.
Suh H, Consiglio A, Ray J, Sawai T, D'Amour KA, Gage FH (2007) In vivo fate analysis reveals the multipotent and self-renewal capacities of Sox2+ neural stem cells in the adult hippocampus. Cell Stem Cell 1:515-528.
Tang C, Wang M, Wang P, Wang L, Wu Q, Guo W (2019) Neural stem cells behave as a functional niche for the maturation of newborn neurons through the secretion of PTN. Neuron 101:32-44.e6.
Valério-Gomes B, Guimarães DM, Szczupak D, Lent R (2018) The absolute number of oligodendrocytes in the adult mouse brain. Front Neuroanat 12:90.
von Bohlen und Halbach O (2011) Immunohistological markers for proliferative events, gliogenesis, and neurogenesis within the adult hippocampus. Cell Tissue Res 345:1-19.
Wang XX, Li JT, Xie XM, Gu Y, Si TM, Schmidt MV, Wang XD (2017) Nectin-3 modulates the structural plasticity of dentate granule cells and long-term memory. Transl Psychiatry 7:e1228.
Willis CM, Nicaise AM, Peruzzotti-Jametti L, Pluchino S (2020) The neural stem cell secretome and its role in brain repair. Brain Res 1729:146615.
Wirenfeldt M, Dalmau I, Finsen B (2003) Estimation of absolute microglial cell numbers in mouse fascia dentata using unbiased and efficient stereological cell counting principles. Glia 44:129-139.
Yassa MA, Stark CEL (2011) Pattern separation in the hippocampus. Trends Neurosci 34:515-525.
Zhou Y, Bond AM, Shade JE, Zhu Y, Davis CO, Wang X, Su Y, Yoon KJ, Phan AT, Chen WJ, Oh JH, Marsh-Armstrong N, Atabai K, Ming G, Song H (2018) Autocrine Mfge8 signaling prevents developmental exhaustion of the adult neural stem cell pool. Cell Stem Cell 23:444-452.e4.

C-Editors: Zhao M, Liu WJ, Li CH; T-Editor: Jia Y